ACS APPLIED NANO MATERIALS

www.acsanm.org

Forum Article

Choline Carboxylic Acid Ionic Liquid-Stabilized Anisotropic Gold Nanoparticles for Photothermal Therapy

Priyavrat Vashisth, Cameron L. Smith, Dhanush L. Amarasekara, Gaya S. Dasanyake, Gagandeep Singh, Claylee M. Chism, Christine M. Hamadani, Tanveer Shaikh, Noah Grovich, Briana Gamboa, Nicholas C. Fitzkee, Nathan I. Hammer, and Eden E. L. Tanner*

Cite This: *ACS Appl. Nano Mater.* 2024, 7, 26332–26343

Read Online

ACCESS | Metrics & More | Article Recommendations | Supporting Information

ABSTRACT: Gold nanoparticles (AuNPs) are commonly used in cancer research due to their unique physical and optical properties. However, current AuNP synthesis methods often involve cytotoxic cationic surfactants such as cetyltrimethylammonium bromide (CTAB). Tedious CTAB replacement methodologies have been used to increase the biocompatibility, further increasing the complexity of synthesizing biocompatible AuNPs and limiting their biomedical applications. To address this issue, we explore cholinium decanoate (CADA) ionic liquid (IL) as a biocompatible stabilizing agent by replacing CTAB using a simple modified seeded method for synthesizing anisotropic AuNPs for photothermal therapy of triple-negative breast cancer cells (MDA-MB-231). The prepared CADA AuNPs showed a quasi-spherical morphology, confirmed by transmission electron microscopy (TEM) and a broad plasmonic absorption band using vis-NIR spectroscopy. CADA AuNPs exhibited excellent in vitro biocompatibility with both MCF-10A (healthy human mammary cells) and MDA-MB-231 cells. We evaluate their in vitro photothermal efficacy against MDA-MB-231 cancer cells, demonstrating significant cell death even at low AuNP concentration (20 μg/mL), low laser power density (0.6 W/cm^2, 808 nm continuous laser), and short irradiation time of 5 min, primarily through apoptosis. Overall, this work represents the first effort in using a modified seeded method for synthesizing biocompatible IL-based anisotropic AuNPs for photothermal therapy, offering a promising avenue for future cancer treatment research using ILs.

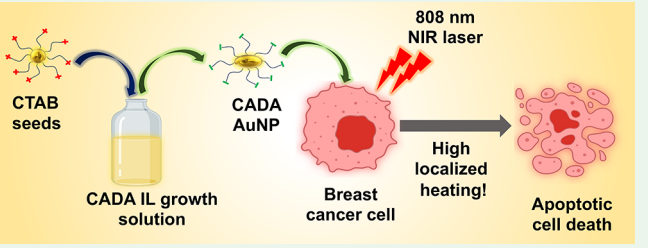

KEYWORDS: *ionic liquids, gold nanoparticles, biocompatibility, seeded method, plasmon resonance, photothermal therapy*

1. INTRODUCTION

Breast cancer is the most prevalent form of cancer in women worldwide, with over 2 million cases and 600,000 deaths reported by 2020.[1] In the United States alone, more than 200,000 invasive breast cancer cases and 50,000 noninvasive cases were reported in 2022.[1] Triple-negative breast cancer represents a particularly aggressive and complex subtype, lacking hormone receptors (progesterone and estrogen) and exhibiting low expression of human epidermal growth factor receptor 2 (HER2). Typical breast cancer cells have overly expressed HER2, progesterone, and estrogen receptor (ER), but triple-negative breast cancer (TNBC) cells are both progesterone and ER-negative and also have a very low HER2 expression, which results in a more aggressive phenotype of breast cancer.[2−5] with higher mortality rates. In the US, TNBC particularly impacts Black and African American women, contributing to the racial disparity in survival from breast cancer. TNBC is typically treated with chemotherapy, a highly nonspecific, nontargeted, and cytotoxic mode of treatment.[6−8] Long and repeated chemotherapy cycles can destroy cancer cells but cause irreversible damage to healthy cells and other severe side effects for patients.[9,10]

To find a suitable alternative to chemotherapy, nanoscale targeted theranostics have been explored, with gold nanoparticles (AuNPs) showing considerable promise in cancer treatment via photothermal therapy (PTT).[11−16] AuNPs possess advantages such as ease of synthesis, surface modifications, and absorption in the biologically relevant near-infrared (NIR) region, suitable for PTT.[17] This minimally invasive and controlled therapeutic approach relies on the intense localized temperature change or hyperthermia-induced killing of cancer cells predominantly via apoptosis or necrosis depending on the degree of temperature change, irradiation time, and laser power density used for conducting the photothermal treatment.[18,19]

Special Issue: Early Career Forum 2024

Received: September 28, 2023
Revised: December 18, 2023
Accepted: December 22, 2023
Published: January 29, 2024

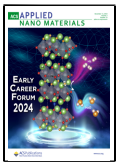

https://doi.org/10.1021/acsanm.3c04645
ACS Appl. Nano Mater. 2024, 7, 26332−26343

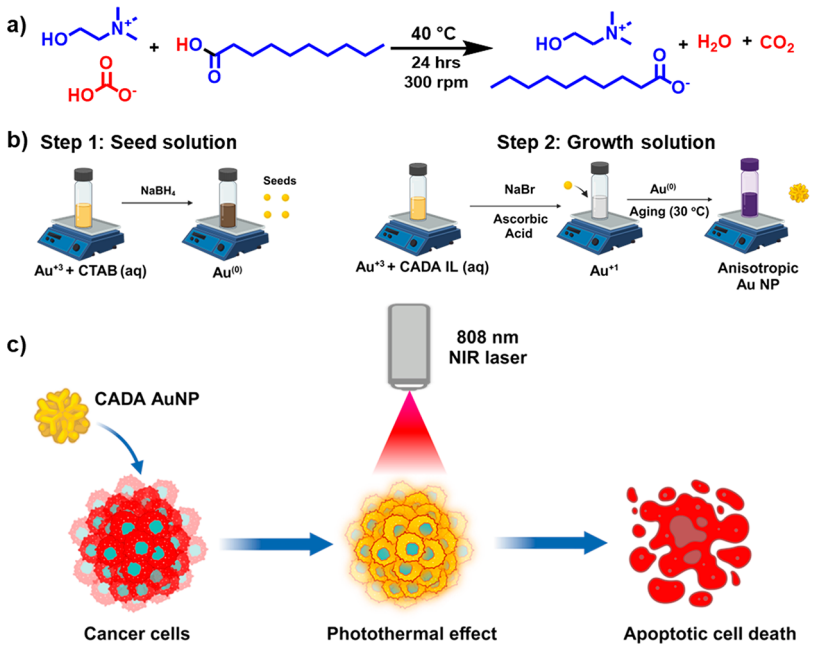

Figure 1. Biocompatible ionic liquids can be used to stabilize gold nanostructures using a modified wetseeded method for photothermal therapy. (a) General scheme for the synthesis of CADA (1:1) IL using a salt metathesis method. The bicarbonate ion abstracts the acidic proton from the carboxyl group of decanoic acid to form the CADA IL with H_2O and CO_2 as the side products, which can be easily removed from the IL by rotatory evaporation and vacuum drying. (b) Schematic for the modified wet seeded method used for the synthesis of CADA AuNP. (c) Schematic representing the overall outlook of photothermal therapy of cancer cells treated using CADA AuNP and a continuous 808 nm NIR laser.

Anisotropic AuNPs like gold nanorods, nanostars, and nanoclusters are the ideal choice for PTT due to their impressive absorption and photothermal conversion efficiencies.[20,21] Although the current anisotropic AuNP syntheses are well-established and reliable in terms of shape control and reproducibility, they still involve the use of cytotoxic cationic surfactants like CTAB.[22−24] Laborious synthetic variations have been undertaken to either replace cationic surfactants from AuNP surface or encapsulate them with molecules like PLGA, PEG, DNA, antigens, or antibodies to enhance their biocompatibility.[25,26]

To address the challenges of CTAB cytotoxicity and replacement methods, we propose using biocompatible ionic liquids (ILs) as biosafe stabilizing agents for anisotropic AuNPs. ILs are comprised of asymmetric cations and anions which are liquid below 100 °C. They offer unique physical and chemical properties, including tunable viscosity, conductivity, and a plethora of manipulatable interionic forces, e.g., hydrogen bonding, dipole−dipole interactions, etc.[27] Imidazolium cation-based ILs and ascorbic acid-based ILs have previously been used in AuNP synthesis, but their applications in cancer therapy are relatively unexplored.[28−32] Recently, ILs comprised of biologically compatible starting materials have been used in nanoparticle synthesis, as antimicrobial agents, for protein stabilization, and in drug delivery applications, expanding the use of ILs from conventional use in catalysis, electrochemistry, and energy applications.[33−41] The tunability of ILs, by altering the chemical composition of the cation and anion, allows the design of surfactants with desired structural and biological features.[42] Bioinspired cholinium-based ILs have exhibited promising biological applications due to choline's vital role in the human nervous system and metabolism, which aids in synthesizing crucial biomolecules for maintaining cellular structures.[43,44]

Herein, we have developed a silver-free modified version of the seeded method to synthesize biocompatible IL-based anisotropic AuNPs for photothermal therapy of MDA-MB-231 cells.[45,46] We employ choline paired with a decanoic acid anion (hereafter called CADA), an FDA-approved medium-chain fatty acid with previously shown antimicrobial and anti-inflammatory properties.[47−49] CADA facilitates the formation of CADA AuNPs with quasi-spherical morphology, as confirmed by scanning electron microscopy (SEM) and transmission electron microscopy (TEM). CADA AuNP demonstrates excellent in vitro biocompatibility with both MCF-10A and MDA-MB-231 cells. The in vitro photothermal efficacy of CADA AuNP was assessed with MDA-MB-231 cancer cells, demonstrating substantial cell death even at a low AuNP concentration (20 μg/mL), low laser power density (0.6 W/cm^2), and a short irradiation time (5 min) predominantly via apoptosis. This work marks the first application of a modified, silver-free, seeded method for synthesizing biocompatible IL-based anisotropic AuNPs for use in photothermal therapy (PTT), bridging the gap between IL-based AuNPs and biomedicine and holding promising potential for future cancer research using ILs.

2. RESULTS AND DISCUSSION

2.1. Synthesis and Characterization of CADA IL and CADA AuNPs. Choline decanoate (CADA) IL was prepared using a one-step salt metathesis procedure in a 1:1 molar ratio, with the general scheme given in Figure 1a. The synthesized IL was characterized using ^{1}H NMR spectroscopy as shown in Figure S1. CADA AuNPs were synthesized using a modified version of the wet-seeded method developed by Murphy et al. and El Sayed et.al, with a detailed procedure given in the Materials and Methods section.[45,46] The first step was kept the same as in a conventional seeded method where small AuNP

https://doi.org/10.1021/acsanm.3c04645
ACS Appl. Nano Mater. 2024, 7, 26332−26343

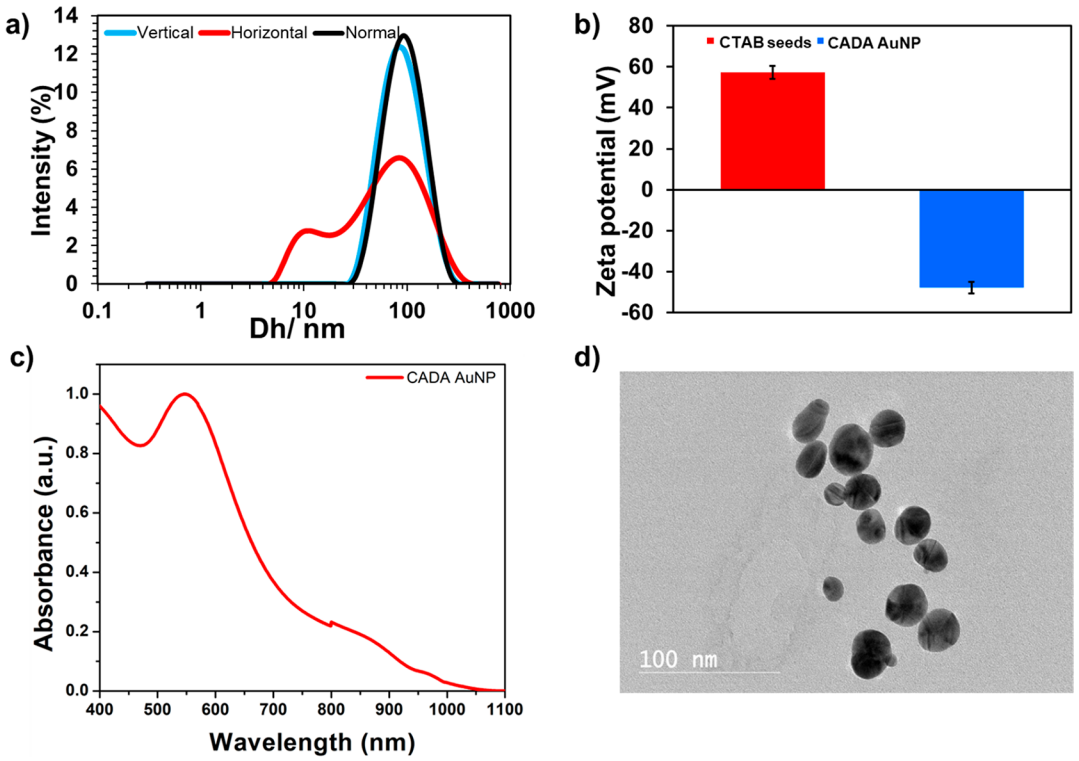

Figure 2. Physical characterization of CADA AuNP highlighting the anisotropic features observed from different measurements. (a) Hydrodynamic diameter distribution of CADA AuNP using different optical filters. The difference in the intensity profiles between horizontal and vertical filters provides evidence for anisotropic AuNPs. (b) Surface charge distribution of AuNPs, CTAB seeds, and CADA AuNPs. The large anionic shift of surface charge from CTAB seeds to final CADA AuNPs suggests the successful replacement of CTAB by the CADA IL. (C) Normalized vis-NIR extinction spectra of CADA AuNP. The broad plasmonic band extending into the NIR region is a characteristic feature of the anisotropic NP population. (D) TEM image of CADA AuNP depicting the anisotropic quasi-spherical nanostructures responsible for the broad absorption observed in the normalized extinction spectra Errors represent the standard deviations from at least three independently prepared samples.

seeds are synthesized by reducing a gold precursor ($HAuCl_4 \cdot 3H_2O$) in CTAB(aq) using sodium borohydride solution. The modification was done in the next step where CADA was used instead of CTAB to serve as the stabilizing agent and provide a template for the anisotropic growth of the AuNPs. Ascorbic acid was added to a 10 mM solution of CADA to serve as a weak reducing agent to reduce Au^{3+}(golden) to Au^{1+}(colorless) in the presence of a small volume of CTAB seeds to initiate the growth of AuNP, schematic shown in Figure 1b.[50] The color of the CADA growth solution changed from colorless to purple, visible to the naked eye, within 5−10 min after the addition of CTAB seeds, indicating the fast growth kinetics of AuNP formation in the presence of ILs. Figure 1c provides a general schematic showing the proposed entry of CADA AuNP into cancer cells followed by NIR laser irradiation and subsequent death of cancer cells via hyperthermia-induced (photothermal effect) induced apoptosis.

Dynamic light scattering (DLS) was used to determine the hydrodynamic diameter of the prepared AuNPs. Horizontal and vertical filters were applied to analyze the anisotropic features, and Figure 2a gives the scattering profiles of CADA AuNP under different polarization settings, where standard DLS measurements assume nanoparticles to be spherical and provide an average hydrodynamic diameter (Dh) based on Brownian motion and the Stokes−Einstein equation. However, for anisotropic nanoparticles, distinct dynamics occur in aqueous solution compared to their spherical counterparts. Anisotropic nanoparticles can undergo both translational and rotational motion, resulting in varying diffusion coefficients. Specifically, the vertical polarizer provides insights into the translational diffusion coefficient of AuNPs and their movement within the solution. Conversely, the horizontal polarizer provides information about the rotational diffusion coefficient, and the difference in their profiles provides a good indication that the CADA AuNPs are anisotropic.[30,51,52]

The hydrodynamic diameters from the size filters were determined as follows: normal (71.9 ± 0.3 nm), vertical (76.2 ± 0.4 nm), and horizontal (37.5 ± 0.4 nm), respectively. The polydispersity index of the AuNPs was measured to be 0.28. The surface charges of the CTAB seeds and CADA AuNPs were measured to be 57 ± 3 and −48 ± 3 mV, respectively, as shown in Figure 2b. The net negative surface charge surface charge of the AuNP suggests that CADA has successfully replaced CTAB. This was further confirmed by ^{1}H NMR spectroscopy, where Figure S1 shows the proton NMR spectrum of CADA, CADA AuNPs, and CTAB, respectively. The overlap of the chemical shifts of the protons of the neat CADA and the CADA AuNPs compared to CTAB confirms the presence of CADA on the surface of AuNPs (peaks at 4.00, 3.42, and 3.11 ppm). The optical properties were then investigated by using absorption spectroscopy. Figure 2c shows the broad absorption band of CADA AuNP with a maximum absorption (λ_{max}) around 545 nm, extending up to 1000 nm in the NIR region, suggestive of an anisotropic shape leading to a surface plasmonic resonance.[13]

To validate the morphology of the CADA AuNPs, scanning electron microscopy (SEM) and transmission electron microscopy (TEM) imaging were conducted. Figure 2d

https://doi.org/10.1021/acsanm.3c04645
ACS Appl. Nano Mater. 2024, 7, 26332−26343

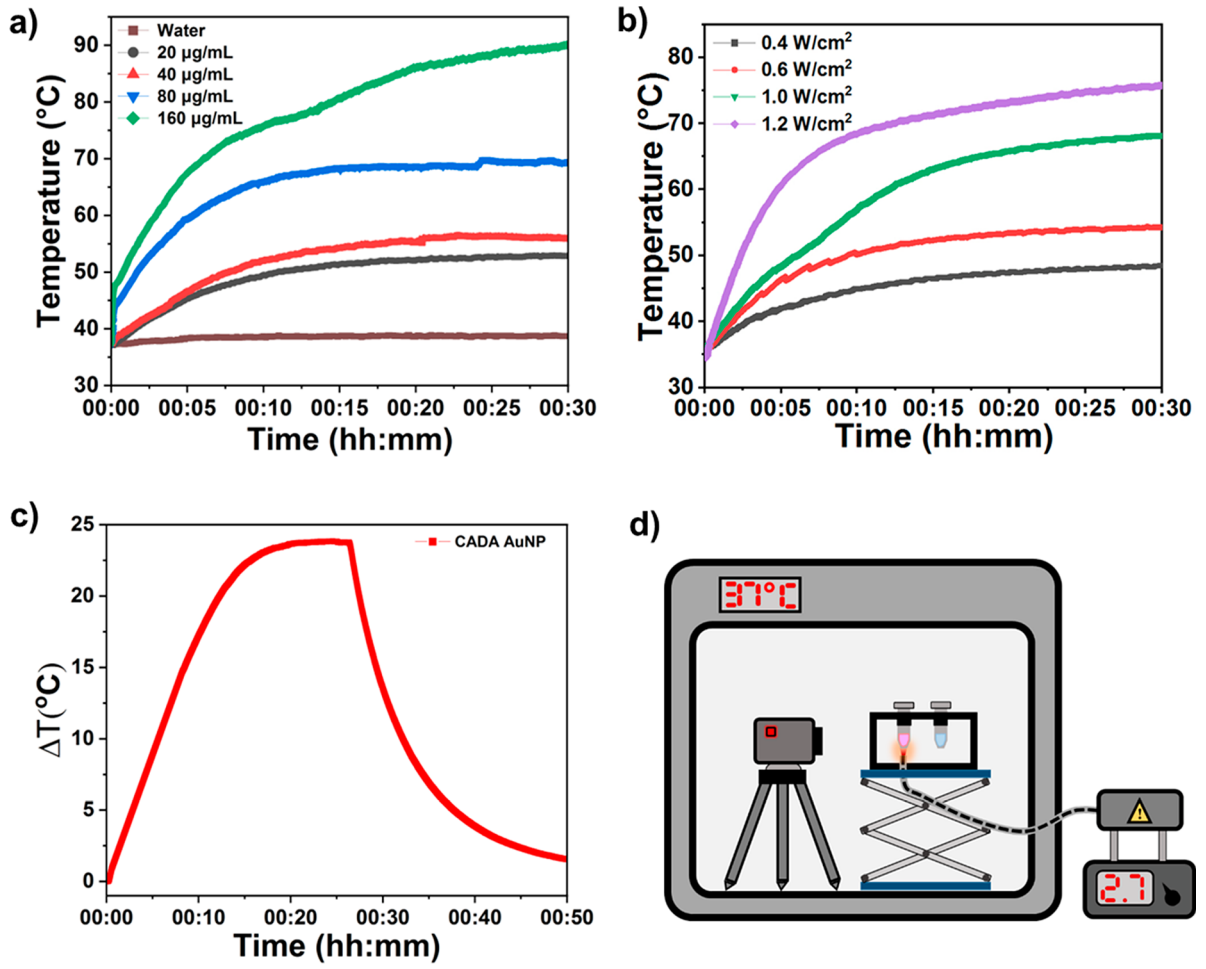

Figure 3. Photothermal performance of CADA AuNPs shows a positive correlation as the temperature change is larger with increasing power density and concentration. Temperature profiles for CADA AuNPs. (a) CADA AuNP concentration scan at a fixed laser power density of 0.6 W/cm^2. (b) Laser power density scan at a fixed concentration of 20 μg/mL. (c) Heating/cooling curve of CADA AuNP at 20 μg/mL and 0.6 W/cm^2. (d) Schematic for the photothermal setup used for conducting the experiments.

illustrates the formation of quasi-spherical nanostructures of the CADA AuNPs, and SEM images can be found in Figure S2 consistent with the broad plasmonic absorption in the Vvs-NIR spectrum, as well as the observed anisotropic characteristics in DLS measurements. CADA AuNPs show a low degree of anisotropy, forming quasi-spherical structures. The low degree of anisotropy is attributed to the fast growth kinetics of the formation of AuNPs, surface charge, and organic species present in the solution. In a typical seed-mediated method, the geometry of the final nanostructures is greatly influenced by the growth medium and especially the anion present in the solution. The resulting particles have high negative surface charge (Figure 2b), so it is likely that the CADA IL adsorbs onto the surface of small AuNP providing nucleation sites for controlled growth. The long hydrophobic chain present in the decanoate anion is likely providing the template for further AuNP growth and acting as a bridging ligand between adjacent AuNPs leading to the formation of quasi-spherical nanostructures.[53,54]

2.2. Photothermal Performance of CADA AuNPs. The photothermal capability of CADA AuNPs was tested thoroughly to study the effect of different experimental conditions using an IR-thermal imaging camera (PI400i, Optris, Portsmouth, NH) and an 808 nm continuous NIR laser. The 808 nm continuous NIR laser was chosen because of its relevance in biological applications, namely, the ability to penetrate tissue to target deep-seated tumors. This occurs because in the NIR region (800−1200 nm) there is minimal absorption interference from other chromophores present in tissues (like water, blood, fat, melanin, etc.), and also, there is reduced scattering. Hence, the AuNPs can effectively absorb the NIR radiation and generate enhanced hyperthermia through the photothermal effect.[55,56]

For CADA AuNP, despite the λ_{max} being around 545 nm (visible region), a broad plasmonic absorption band extends up to the NIR region. In cases where AuNPs are in close proximity, the wavelength of maximum absorption tends to shift toward higher wavelengths through collective surface plasmon resonance. This spectral adjustment enhances the efficacy of NIR radiation absorption.[57] To investigate the AuNP concentration-dependent temperature change, a series of different CADA AuNP concentration solutions (0−160 μg/mL) were irradiated with a fixed laser power density of 0.6 W/cm^2 for a standardized duration of 30 min. Figure 3a shows the temperature changes in each case. The irradiation time for the physical characterization of CADA AuNP was performed at 30 min to test their long-term photothermal performance to provide insight into the capacity of the material to withstand longer irradiation times. Notably, a rapid temperature increase occurs within the first 5 min (shown in Figure S3), followed by

https://doi.org/10.1021/acsanm.3c04645
ACS Appl. Nano Mater. 2024, 7, 26332−26343

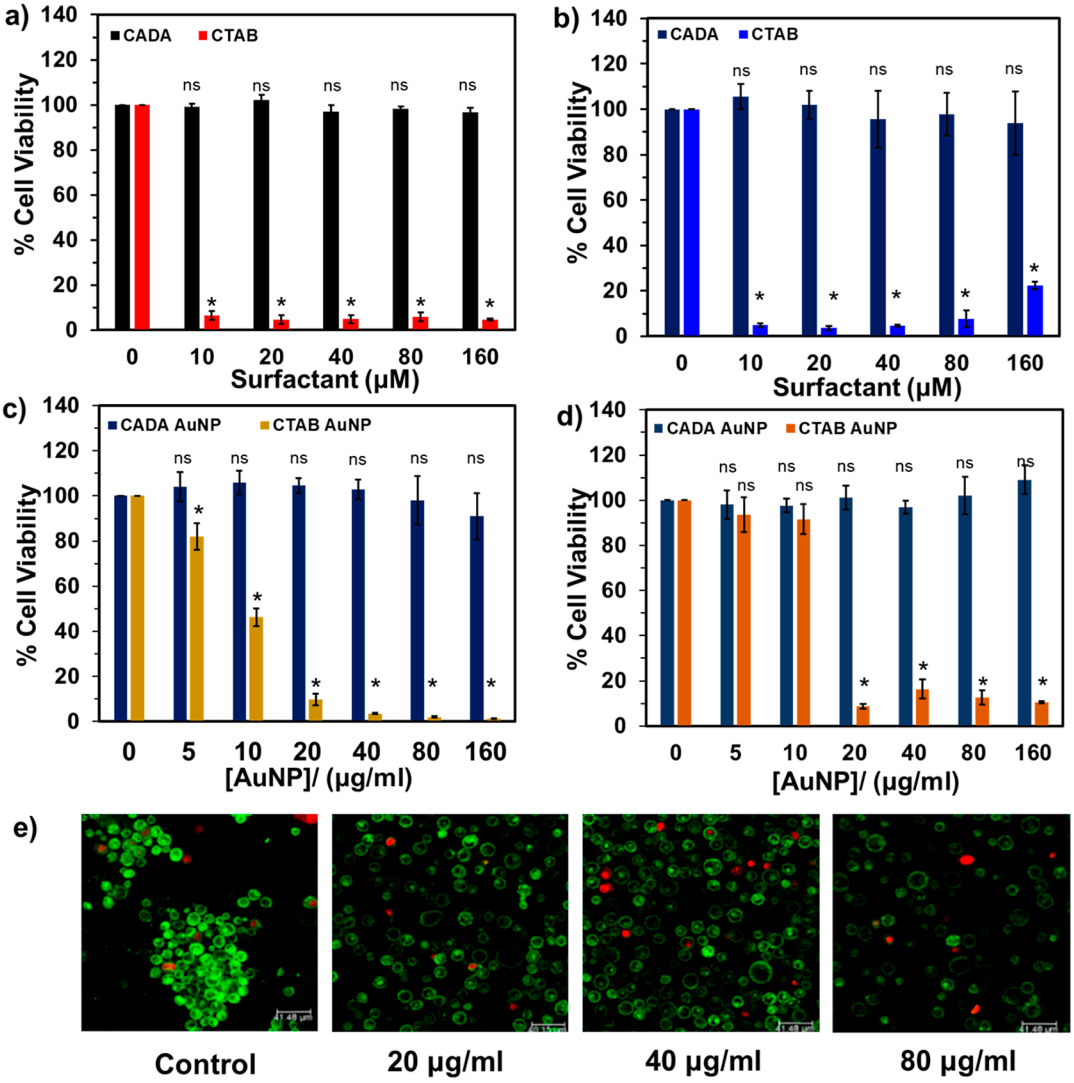

Figure 4. CADA IL and CADA AuNP have shown superior biocompatibility as compared to CTAB and CTAB AuNP for both healthy cells and breast cancer cells without any laser ablation. The in vitro cell viabilities of adherent cells incubated with varying surfactant concentrations for 24 h were assessed by a Cell Titer-Glo(R) luminescent cell viability kit. (a) MCF-10A cell viability, (b) MDA-MB-231 cell viability. In vitro cell viabilities of adherent cells incubated with varying CADA AuNP concentrations for 24 h assessed by CellTiter-Glo(R) luminescent cell viability kit. (c) MCF-10 A, (d) MDA-MB-231. (e) Live cell confocal imaging of MDA-MB-231 cells incubated with increasing CADA AuNP concentrations (20, 40, and 80 μg/mL). Errors represent the standard deviation from at least three independently prepared samples. Statistical significance was performed by two-tailed Student *t*-test by comparing each concentration to the negative control, $n = 3$, mean ± SD, $* = p < 0.05$, ns = nonsignificant.

a subsequent plateau at a constant temperature value. This gives the maximum temperature reached at that concentration. A discernible positive correlation was observed between the AuNP concentration and degree of temperature change, which was anticipated as higher concentration implies more AuNPs, i.e., more surface plasmons, thus facilitating enhanced NIR light absorption and localized heat generation, resulting in greater temperature changes.

Additionally, photothermal experiments were performed at a fixed concentration of 20 μg/mL, employing varying laser power densities within 0.4−1.4 W/cm^2 range. Figure 3b shows the respective temperature changes, and again, a similar positive correlation is observed wherein higher laser power density led to greater changes in temperature. Furthermore, the photothermal efficiency of the CADA AuNPs was calculated at the same concentration (20 μg/mL). Figure 3c shows the observed heating/cooling curve obtained by switching off the laser after 25 min of irradiation and allowing the solution to cool down to 37 °C. The temperature difference was used to calculate the photothermal conversion which was found to be 50.5%; detailed calculations can be found in the SI. The photothermal efficiency (PTE) of CADA AuNPs is consistent with the efficiencies of CTAB AuNPs and other anisotropic AuNPs synthesized via alternative methods which are usually in the range of 50%−70%.[23,58−60] However, a direct comparison is challenging, as PTE is influenced by numerous variables including the synthesis method, coating material, nanoparticle size and shape, and laser power.[61] Notably, the observed PTE of our materials is substantial, demonstrating robust selectivity and effective induction of apoptosis in cells through irradiation.

Figure 3d provides a general schematic of the photothermal setup used for conducting the experiments. Based on the insights given by photothermal experiments, a laser power

https://doi.org/10.1021/acsanm.3c04645
ACS Appl. Nano Mater. 2024, 7, 26332−26343

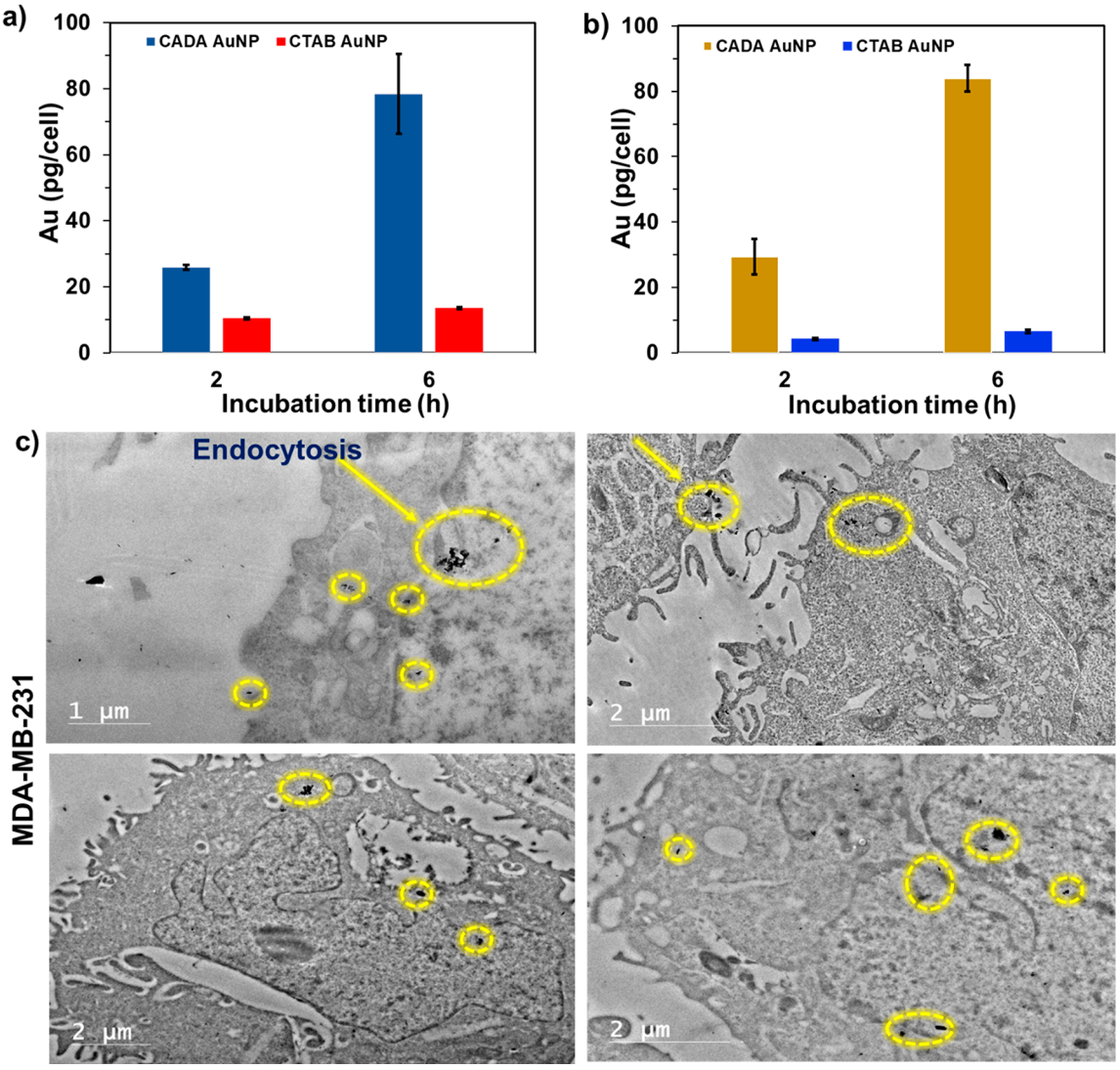

Figure 5. Cellular uptake analysis reveals that CADA AuNP shows higher uptake compared to CTAB AuNP in MDA-MB-231 and MCF-10A cells, which increases significantly from 2 to 6 h for CADA AuNP for both cell lines, whereas a little change is seen in the case of CTAB AuNP. Amount of CADA AuNP and CTAB AuNP (pg/cell) present in (a) MCF-10A, (b) MDA-MB-231 cells, quantified using ICP-MS measurements after incubation periods of 2 and 6 h, respectively. (c) TEM micrographs of MDA-MB-231 cells incubated with CADA AuNP after 6 h incubation showing the cellular uptake through endocytosis into the cytoplasm. Errors represent the standard deviation from the mean for the triplicate measurements.

density of 0.6 W/cm^2 and an irradiation time of 5 min were chosen as the ideal parameters to conduct the in vitro photothermal studies to meet the clinically approved laser power limits.

2.3. In Vitro Biocompatibility of Surfactants and AuNPs. Initially, the in vitro biocompatibility of CADA and CTAB surfactants was investigated using a CellTiter-Glo luminescent cell viability assay to test their inherent biocompatibility toward both MCF-10A and MDA-MB-231cell lines. Figure 4a and b gives the % viability for respective cell lines at six different surfactant concentrations (0−160 μM). CADA outperformed CTAB in both cases, as CTAB was found to be toxic even at a low concentration of 10 μM for both MCF 10A and MDA-MB-231 cells. Numerous studies can also be found in the literature confirming the cytotoxic nature of CTAB.[62,63] In contrast, the CADA IL showed excellent biocompatibility, with cell viability higher than 90% even at the highest concentration measured for both MCF-10A and MDA-MB-231 cell lines (97 ± 2% for MCF-10A and 94 ± 13% for MDA-MB-231 at 160 μM). Note that the increase in viability seen with CTAB at 160 μM is likely to be due to the formation of microstructures (Figure S9), which reduces the effective concentration in solution.[64] Next, the in vitro biocompatibility of CADA AuNP and CTAB AuNP (physical characterization including size, surface charge, and vis-NIR absorption is given in Figure S4) toward MCF-10A and MDA-MB-231 cells was quantified using the same luminescent cell viability assay as mentioned above. The adherent cells were incubated with different concentrations of CADA AuNP and CTAB AuNP, and viability was calculated against a negative control as depicted in Figure 4c and d. CADA AuNP also exhibited excellent biocompatibility, with cell viabilities exceeding 90% for both cell lines as expected, whereas CTAB AuNP displayed high cytotoxicity against both healthy and cancer cells. Furthermore, live/dead cell staining was used to assess the biocompatibility of CADA AuNPs

https://doi.org/10.1021/acsanm.3c04645
ACS Appl. Nano Mater. 2024, 7, 26332−26343

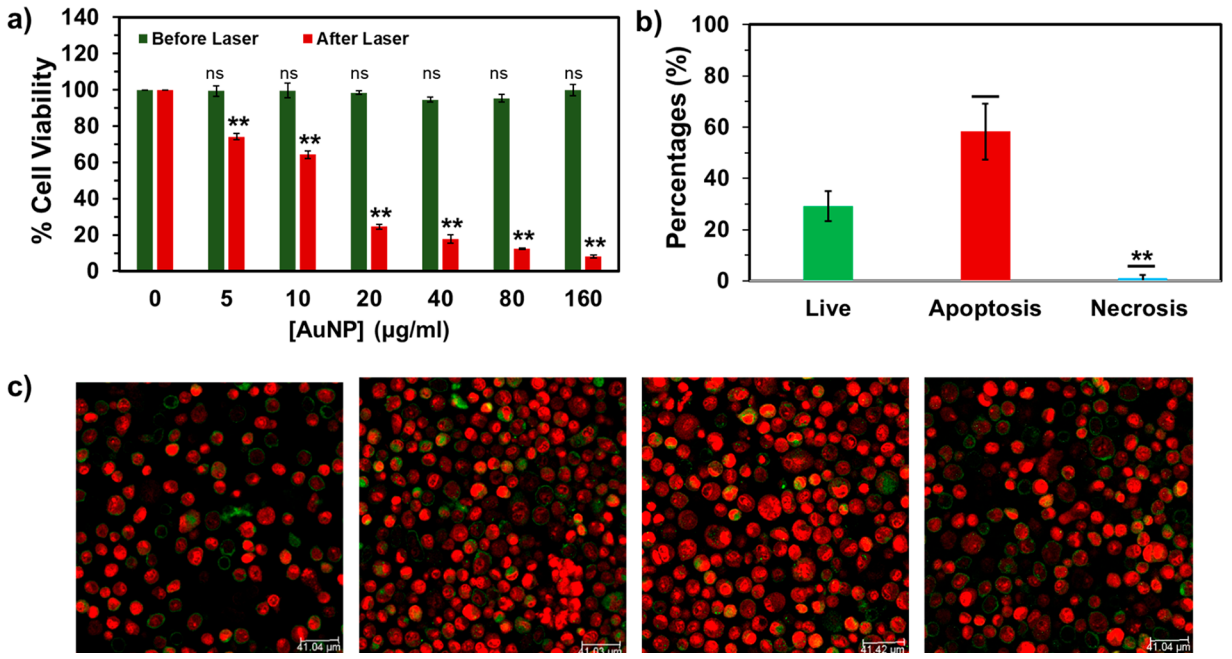

Figure 6. In vitro photothermal studies of MDA-MB-231 cells reveal that significant cell death has occurred post-NIR laser irradiation, and the prominent mechanism of cell death is found to occur via apoptosis. (a) CADA in vitro cell viability of MDA-MB-231 adherent cells incubated with varying CADA AuNP concentrations for 24 h, assessed by CellTiter-Glo(R) luminescent cell viability kit. Cell viability is measured after NIR (808 nm) laser treatment of cells at 0.6 W/cm^2 for 5 min. (b) % of apoptosis/necrosis induced by CADA AuNP (20 μg/mL) in MDA-MB-231 cells after photothermal therapy at the same parameters. (c) Live cell confocal images of MDA-MB-231 cells treated with CADA AuNP (20 μg/mL) after NIR laser irradiation for 5 min for four independent samples. Errors represent the standard deviation from at least three independently prepared samples. Statistical significance was performed by two-tailed Student *t*-test compared to the negative control for (a) and comparing and apoptosis and necrosis in (b), $n = 3$, mean ± SD, ** = $p < 0.01$, ns = nonsignificant.

toward MDA-MB-231 cells. CellBrite Cytoplasmic Membrane Dye was used for staining live cells, giving it a characteristic green fluorescence signal. Propidium iodide (PI) was used for dead cells with a red fluorescent signal. Figure 4e shows the live cell confocal imaging of MDA-MB-231 cells incubated with increasing CADA AuNP concentrations (20, 40, and 80 μg/mL); the predominant green fluorescent signal confirms the biocompatibility of CADA AuNP. These results confirm that the prepared nanostructures demonstrate no inherent cytotoxicity and are deemed safe to proceed with in vitro photothermal studies.

2.4. Cellular Uptake of CADA AuNPs. To evaluate the cellular uptake efficiency of CADA AuNP compared to CTAB AuNPs, we employed inductively coupled plasma−mass spectrometry (ICP-MS) measurements to quantify the intracellular amount of Au inside the MDA-MB-231 cells and MCF-10A cells after incubation with both CADA AuNPs and CTAB AuNP. The incubation was done at a fixed AuNP concentration (20 μg/mL) for duration of 2 and 6 h, respectively. Figure 5a and b depict the Au content in the respective cell lines. CADA AuNP showed significantly higher cellular uptake when compared with CTAB AuNP in MDA-MB-231 cells. Interestingly, the AuNP uptake increased much more for CADA AuNP from 2 h of incubation (29.5 ± 5.4 pg/cell) to 6 h (84.0 ± 4.0 pg/cell) incubation. In contrast, CTAB AuNPs showed minimal change in AuNP uptake after 2 h (4.2 ± 0.2 pg/cell) and 6 h (6.5 ± 0.4 pg/cell) incubation periods. Similar trends were observed in the case of the MCF-10A cells. For CADA AuNPs, the Au contents were 25.8 ± 0.7 and 78.4 ± 12.0 pg/cell after 2 and 6 h incubation, respectively, whereas for CTAB AuNP the contents were 10.4 ± 0.3 pg/cell at 2 h and 13.5 ± 0.4 pg/cell 6 h incubation periods. The detailed Au concentrations (parts per billion) in both cell lines is given in Figure S5 and Table S2 in SI. In our case, CADA AuNPs are cytocompatible toward both MCF-10A and MDA-MB-231 cell lines (Figure 4c and d) and anionic in nature (Figure 2b). The decanoate anion, with its long hydrophobic chain, can further facilitate membrane permeation.[65,66] Anionic NPs can interact with the cationic lipid domains of the cell membrane which presumably leads to their further internalization into the cells using the endocytosis pathway.[67−69] Figure 5c evidences the uptake of CADA AuNP into the cytoplasm of MDA-MB-231 cells through endocytosis.[70,71] These results demonstrate that the CADA IL enhances the cellular uptake of AuNP in both breast cancer cells and healthy breast cells.

2.5. In Vitro Photothermal Performance of CADA AuNPs. In order to evaluate the in vitro PTT efficacy, adherent MDA-MB-231 cells were incubated with varying concentrations of CADA AuNPs (0−160 μg/mL) and subsequently exposed to continuous 808 nm NIR laser irradiation (0.6 W/cm^2) for 5 min. For in vitro experiments, the irradiation time is kept at a minimum, just enough to induce controlled cell death via apoptosis. From the photothermal characterization of CADA AuNP (Figure 3), it was determined that the temperature rises rapidly within the first 5 min of laser irradiation (about 10 °C). This rapid increase in temperature is sufficient to induce cancer cell death.[72,73]

After a 24 h incubation (37 °C, 5% CO_2), cell viability was measured using a luminescent cell viability assay to quantify the postlaser treatment cellular death process. Figure 6a represents the respective cell viability measured against a negative control. The viability of cancer cells decreased with increasing AuNP concentration, i.e., 74.1% at 5 μg/mL, 64.2% at 10 μg/mL, 24.6% at 20 μg/mL, 17.7% at 40 μg/mL, 12.3%

https://doi.org/10.1021/acsanm.3c04645
ACS Appl. Nano Mater. 2024, 7, 26332−26343

at 80 μg/mL, and 8.1% at 160 μg/mL. Figure 6a illustrates the respective cell viability against a negative control, revealing a significant decrease in viability at 20 μg/mL CADA AuNP, making it a suitable concentration to induce cancer cell death via photothermal effect. Moreover, to further analyze the in vitro photothermal performance of CADA AuNP, live/dead cell imaging was done using confocal laser scanning microscopy at three different AuNP concentrations, i.e. 20, 40, and 80 μg/mL. Figure 6c illustrates the images taken after laser treatment (20 μg/mL), with most cells displaying the red fluorescent signal, confirming the photothermal efficacy of CADA AuNPs, and a similar trend was observed after laser treatment for 40 and 80 μg/mL, as shown in Figure S6. Further, CADA AuNP showed excellent stability after laser ablation, tested by measuring the change in size, surface charge, and absorption properties as shown in Figure S7 and Table 3.

To further assess the photothermal performance of the CADA AuNP, an Annexin V-FITC/PI Apoptosis Detection Kit was used to identify the photothermally induced cellular death pathway in cancer cells. MDA-MB-231 cells were incubated with 20 μg/mL of CADA AuNP, followed by PTT treatment (0.6 W/cm^2 for 5 min) and Annexin V-FITC/PI staining as per the vendor's protocol. Fluorescence-activated cell sorting (FACS) measurements were performed in triplicate to quantitatively determine apoptosis and necrosis. Figure 6b displays the percentage of live, apoptotic, and necrotic MDA-MB-231 cells after PTT treatment; detailed information and gating parameters can be found in Figure S8. These results emphasize the specificity of CADA AuNP-based photothermal therapy in inducing controlled cancer cell death primarily via apoptosis and present biocompatible ionic liquids as viable contenders for cytocompatible surfactants of anisotropic AuNPs.

3. CONCLUSIONS

In this work, we have successfully synthesized biocompatible CADA AuNPs using a modified silver-free seeded method. Comprehensive characterization techniques confirmed the physical properties of CADA AuNPs, revealing a net negative surface charge and anisotropic geometry. CADA AuNP demonstrated excellent in vitro biocompatibility toward both MCF-10A and MDA-MB-231 cell lines. Remarkably, CADA AuNPs showed impressive photothermal properties even at a low AuNP concentrations (20 μg/mL) and low laser power density (CW 808 nm, 0.6 W/cm^2). In vitro photothermal studies were performed on MDA-MB-231 cells using the same parameters, and the results from cell viability measurements, live/dead cell imaging, and apoptosis/necrosis detection demonstrated significant controlled cell death after only 5 min of laser ablation via apoptosis. This compelling evidence underscores the efficacy of CADA AuNPs in inducing cancer cell death through photothermal effects. In summary, this study presents a novel approach to utilize biocompatible ionic liquids as stabilizing agents for the synthesis of biologically relevant AuNPs, specifically tailored for the treatment of triple-negative breast cancer cells using photothermal therapy. The successful outcomes and well-characterized properties of CADA AuNPs provide a promising avenue for the future development of targeted and effective therapeutic strategies for breast cancer treatment.

5. MATERIALS AND METHODS

Reagents. Choline bicarbonate (80% in H_2O); decanoic acid (≥98.0%); Emsure tetrachloroauric(III) acid trihydrate, 99.5%; L-ascorbic acid, 99%; sodium bromide, BioXtra, ≥99.0%; silver nitrate, ACS reagent, ≥99.0%; and deuterium oxide, 99 atom % D were purchased from Sigma-Aldrich. Ultrapure Milli-Q water was obtained from a Millipore Milli-Q purifier (#Milli-Q IQ 7000). Live/Dead Cell Staining Kit, Mammalian, was purchased from ApexBio. CellBrite Cytoplasmic Membrane Dye was purchased from Biotium. Annexin V-FITC/PI Apoptosis Detection Kit was purchased from MedCheExpress USA.

Methods. *Synthesis of Cholinium Decanoate Ionic Liquid (CADA IL).* CADA IL was synthesized by using a one-step salt metathesis reaction. Decanoic acid and cholinium bicarbonate were mixed in a 1:1 molar ratio. First, an appropriate amount of decanoic acid was weighed and transferred into a 100 mL round-bottom flask followed by dropwise addition of choline bicarbonate solution at a constant stirring rate of 300 rpm at 40 °C. The mixture was allowed to stir for 24 h to complete the ionic liquid synthesis. After 24 h, the IL was dried by using a rotary evaporator (15 mbar, 60 °C for 2 h), and the IL was further dried in a vacuum oven (60 °C for 48 h) to remove any residual water content. A Karl Fischer coulometric titration was performed to calculate the water content in the dried IL. The IL was characterized using ^{1}H NMR spectroscopy, for which details are provided in the Supporting Information.

Synthesis of CADA AuNP. The CADA AuNPs were synthesized using a modified version of the wet-seeded method developed by Murphy et al. and El Sayed et al.[45,46] In the first step, a seed solution was prepared by the reduction of $HAuCl_4$ $3H_2O$ solution (25 μM) in 5 mL of CTAB (aq) using an ice-cold sodium borohydride solution (0.6 mL portion of 10 mM solution diluted to 1 mL using ice-cold water) to yield small AuNP seeds at 1200 rpm for 1 min. The seed solution was allowed to age at room temperature for at least 30 min. In the next step, 100 μL of NaBr solution (100 mM) was added to CADA growth solution (5 mL,10 mM), followed by the addition of $HAuCl_4$ $3H_2O$ solution (25 μM) at 1200 rpm. The solution was allowed to stir for 1 min. Then, 30 μL of ascorbic acid solution (70 mM) was added to the growth solution. Finally, 10 μL of seed solution was quickly injected into the growth solution. The stirring was stopped after 1 min to initiate the growth of anisotropic AuNPs.

Synthesis of CTAB AuNP. The CTAB AuNPs were synthesized using the wet-seeded method developed by Murphy et al. and El Sayed et al.[45,46] In the first step, a seed solution was prepared by the reduction of $HAuCl_4{\cdot}3H_2O$ solution (25 μM) in 5 mL of CTAB (0.1 M, aq) using an ice-cold sodium borohydride solution (0.6 mL portion of 10 mM solution diluted to 1 mL using ice-cold water) to yield small AuNP seeds at 1200 rpm for 1 min. The seed solution was allowed to age at room temperature for at least 30 min. In the next step, a growth solution prepared by mixing 5 μL of $AgNO_3$ (45 mM) was added to CTAB growth solution (5 mL, 0.1M), followed by the addition of $HAuCl_4{\cdot}3H_2O$ solution (25 μM) at 1200 rpm. The solution was allowed to stir for 1 min. Then, 45 μL of ascorbic acid solution (70 mM) was added to the growth solution. Finally, 10 μL of seed solution was quickly injected into the growth solution. The stirring was stopped after 1 min to initiate the growth of the anisotropic gold nanorods. Physical characterization of CTAB AuNP can be found in Figure S4 and Table S1.

Characterization. *Dynamic Light Scattering (DLS) and Surface Charge.* The average hydrodynamic diameter of the prepared CADA AuNP was measured using a Zetasizer Pro, NanoZS (Malvern Instruments, UK). Surface charge measurements were performed on the same instrument using a disposable zeta cell (DTS1070). The DLS samples were prepared by mixing 100 uL of a CADA AuNP solution with 900 uL of Milli-Q water. Size and surface charge measurements were performed in triplicate to calculate the average value with each reading averaged from 15 internal runs. Errors represent the standard deviation from at least three independently prepared samples.

https://doi.org/10.1021/acsanm.3c04645
ACS Appl. Nano Mater. 2024, 7, 26332−26343

Vis-NIR Absorption. The vis-NIR absorption of the prepared CADA AuNP was measured using a double reference Cary 5000 spectrophotometer (Cary 5000 UV−vis-NIR, Agilent).

Scanning Electron Microscopy (SEM). CADA AuNPs were prepared as described above, with the AuNPs being centrifuged at 12,000 rpm for 45 min. The supernatant was discarded, and 10 μL of AuNP solution was diluted to 1 mL using Milli-Q water. Then, 10 uL of the AuNP solution was drop cast onto plasma-cleaned 9.5 × 9.5 mm cylinder aluminum SEM sample stubs (JEOL, #10-005110-50). Samples were allowed to dry overnight at 4 °C under ambient conditions in an airtight environment to prevent dust deposition. The following day, all samples were then sputter coated with palladium to enhance imaging contrast (16.5 mm, 35 mA, 200 s). Images were taken using a JSM-7200 FLV field-emission scanning electron microscope (FESEM).

Transmission Electron Microscopy (TEM) of CADA AuNP and MDA-MB-231 Cells. Aliquots of 5 μL of 24 μg/mL of CADA AuNPs solution were deposited on Formvar-coated copper grids. The excess liquid was wicked away, and the remaining thin film on the grid was allowed to dry for 24 h in a desiccator. Then, imaging was performed. The cells were fixed in a primary fixative agent (2% paraformaldehyde + 2.5% glutaraldehyde + 2 mM $CaCl_2$ in 0.1 M sodium cacodylate buffer pH 7.4) for 2 h at room temperature. Subsequently, they were washed and postfixed with 1% osmium tetroxide for 1 h. Afterward, the cells were washed again and dehydrated in a graded series of ethanol, starting from 30% and gradually increasing to 100% ethanol. Finally, the dehydrated cells were immersed in 100% epoxy and polymerized at 60 °C for 1−2 days. The cells were sectioned using an ultramicrotome and subsequently deposited on Formvar-coated copper grids. After sectioning, the grids were allowed to dry for 2 h in a desiccator. TEM imaging was performed by using a JEOL 2100 TEM with an accelerating voltage of 200 kV to obtain clear images.

Photothermal Performance and Photothermal Efficiency. The photothermal ability of the CADA AuNP was evaluated using an 808 nm NIR laser, and the temperature changes were recorded by an infrared thermal camera (PI400i, Optris, Portsmouth, NH). To study the effect of AuNP concentration, a series of 1 mL CADA AuNP solutions was prepared (0−160 μg/mL)) in sterile 1.5 mL polypropylene snap cap microcentrifuge tubes (Celltreat, part number: 229443), irradiated at 600 mW/cm^2 power density for 30 min. Laser power density-dependent experiments were performed at a fixed concentration of 20 μg/mL. The sample was irradiated for 30 min, and the temperature changes were recorded using the thermal camera to obtain the temperature profiles. The photothermal conversion efficiency of CADA AuNP (20 μg/mL) was calculated at 600 mW/cm^2. Then, 1 mL of CADA AuNP (20 μg/mL) was irradiated continuously for 40 min (at 37 °C). After that, the laser was switched off, and the sample was allowed to cool down (back to 37 °C). THen, 1 mL of deionized water was irradiated at similar conditions for reference. The difference between the reference solution's temperature change and CADA AuNP temperature change was used to calculate the photothermal efficiency; detailed calculations are given in the Supporting Information.

In Vitro Biocompatibility Assay (CADA AuNP and Surfactant Biocompatibility). MCF-10A (human epithelial cells, tissue: breast; mammary gland) and MDA-MB231 (human epithelial cancer cells, tissue: breast; mammary gland) cell lines were obtained from ATCC and used to assess the biocompatibility of CADA AuNP. HyClone Dulbecco's Modified Eagle Medium (DMEM)/F12 1:1: liquid; Dulbecco's phosphate buffered saline (DPBS), sterile, 7.0−7.6, without calcium and magnesium, liquid; and trypsin-EDTA (#SH30042.01) were obtained from Cytiva Life Sciences. Penicillin-streptomycin, fetal bovine serum (FBS), and Cholera toxin from *Vibrio cholerae* were obtained from Sigma-Aldrich. Mammary epithelial cell growth medium (MEGM) BulletKit was purchased from Lonza. CellTiter-Glo Luminescent cell viability assay was purchased from Promega Corporation. MDA-MB 231 cells were cultured in DMEM/F12 with 1% penicillin-streptomycin and 10% v/v FBS. MCF-10A cells were cultured in MEGM medium supplemented with 10% v/v FBS, 100 ng/mL cholera toxin, 1% penicillin-streptomycin (penstrep), 20 ng/mL epidermal growth factor, 500 ng/mL hydrocortisone, 5% Chelex-treated horse serum, and 0.01 mg/mL human insulin.

The MCF-10A and MDA-MB-231 cells were cultured in cell culture-treated 96-well plates (1.5 × 10^4 cell density per well) at 37 °C in a 5% humidified CO_2 incubator. At ∼80% confluency, the cell media was removed and replaced with CADA AuNPs (0−160 μg/mL) dispersed in fresh cell medium followed by incubation for another 24 h. After 24 h, the cell medium was replaced with 100 uL of fresh medium, and 100 μL of CellTiter-Glo(R) luminescent cell viability reagent was added to each well. The 96-well plate was incubated for another 15 min at 37 °C. Finally, the luminescence of each well was measured using a microplate reader (Biotek H1 Synergy Hybrid Multimode). The percentage of cell viability was calculated against a negative control (0 μg/mL).

Cellular Uptake Assay. The cellular uptake of CADA AuNP was evaluated by using ICP-MS. MCF-10A and MDA-MB-231 cells were cultured in 6-well polystyrene tissue culture-treated plates (1 × 10^5 cells/well) at 37 °C in a 5% humidified CO_2 incubator. At ∼80% confluency the cell media was removed and replaced with CADA AuNPs (20 μg/mL) dispersed in fresh cell medium followed by incubation for 2 and 6 h. After respective incubation periods, the medium was removed, and the cells were washed three times (500 μL) with DPBS buffer to remove any free AuNPs. The cells were detached by using EDTA-Trypsin and collected by centrifugation (120*g* for 10 min at 4 °C). The cells were digested using aqua regia, and the amount of Au (in different samples) was calculated using ICP-MS.

In Vitro Photothermal Treatment/Cell Viability Postphotothermal Treatment. MDA-MB-231 cells were cultured in cell culture-treated 96-well plates (1.5 × 10^4 cells/well) with maximum well/reservoir volume of 0.37 mL at 37 °C in a 5% humidified CO_2 incubator at ∼80% confluency; the cell media was removed and replaced with CADA AuNPs (0−160 μg/mL) dispersed in fresh cell medium followed by incubation for another 24 h. After 24 h, the cell medium was replaced with 100 μL of fresh medium, and each well was then irradiated using an 808 nm laser (600 mW for 5 min at 37 °C). After laser treatment, the 96-well plate was further incubated for another 24 h. After 24 h, the cell medium was replaced by 100 μL of fresh medium, and 100 μL of CellTiter-Glo(R) luminescent cell viability reagent was added to each well. The 96-well plate was incubated for another 15 min at 37 °C. Finally, the luminescence of each well was measured using a microplate reader (Biotek H1 Synergy Hybrid Multimode). The percentage cell viability was calculated against a negative control (MDA-MB-231 cells treated with CADA AuNP (0−160 μg/mL) without laser treatment).

Live/Dead Cell Imaging (Live Cell Confocal Imaging). MDA-MB-231 cells were cultured in 6-well polystyrene tissue culture-treated plates (1 × 10^5 cells/well) at 37 °C in a 5% humidified CO_2 incubator. At ∼80% confluency, the cell medium was removed and replaced with CADA AuNPs (20, 40, and 80 μg/mL) dispersed in fresh cell medium followed by incubation for another 6 h. After 6 h, the cell medium was removed, and cells were washed three times (500 μL) with DPBS buffer to remove any free AuNPs. The cells were detached by using EDTA-Trypsin and collected by centrifugation (120*g* for 10 min at 4 °C) as a pellet. The cell pellet was irradiated with an 808 nm laser (600 mW/cm^2 for 5 min). After laser irradiation, the respective cell pellets were redispersed in 1 mL of fresh cell media. The cell suspension was stained with CellBrite Cytoplasmic Membrane Dye (10 μL Bright Green mixed in 5 mL of fresh 10% FBS cell media) for visualizing live cells and propidium iodide (0.25 μM) for dead cells. Briefly, 300 μL of both PI and CellBrite dye solutions were mixed together. For staining, 300 μL of dye mixture was added to 20 μL of cell suspension, followed by 15 min of incubation in the dark at 37 °C. After that, the cells were washed with DPBS buffer (300 μL × 3). Finally, 20 μL of stained cells were placed in 8-well plate for live cell confocal imaging. All images were taken using a confocal Leica SP8X under a 63× oil immersion lens.

Apoptosis/Necrosis Detection. Annexin V-FITC/PI Apoptosis Detection Kit (MedChemExpress USA) was used to evaluate the

https://doi.org/10.1021/acsanm.3c04645
ACS Appl. Nano Mater. 2024, 7, 26332−26343

induced cell death mechanism post-NIR laser treatment of cells. MDA-MB-231 cells were cultured using the same protocol as that mentioned in the cellular uptake section. The cell pellets were irradiated by the NIR laser (808 nm, 600 mW/cm^2 for 5 min). After laser treatment, the given protocol (MedChemExpress USA) was followed to prepare the samples for FACS measurements. Briefly, cells were detached by using Trypsin (without EDTA) and collected in the form of a pellet by centrifugation at 1000*g* for 5 min, after which the supernatant was discarded. The cells were further washed with 1 mL of precooled PBS, resuspended, and centrifuged at 1000*g* for 5 min, and the supernatant was discarded again. The cells were resuspended in 195 μL of binding buffer, followed by the addition of 5 μL of Annexin V-FITC and 10 μL of PI stain, after which the samples were mixed gently. The samples were then incubated at room temperature for 10−20 min in the dark. Finally, the FACS measurements were performed on an Attune NxT acoustic focusing cytometer (Model #AFC2) to calculate the percent apoptosis and necrosis.

Statistical Analysis. Statistical analysis was done using Microsoft Excel 2021, and all data are presented as the mean value ± standard deviation of the mean obtained through three independent experiments. The error for Figure 5a represents standard error of the mean. Comparison between the two groups is done by two-tailed critical student's *t*-test.

■ ASSOCIATED CONTENT

Supporting Information

The Supporting Information is available free of charge at https://pubs.acs.org/doi/10.1021/acsanm.3c04645.

^{1}H NMR characterization of CADA IL, CADA AuNPs, and CTAB. SEM images and heating profiles for CADA AuNPs. Physical characterization of CTAB AuNP, Au content in cells from ICP-MS measurements, additional live cell confocal images of MDA-MB-231 cells after laser irradiation at different concentrations for CADA AuNPs. Physical characterization of CADA AuNPs before and after laser irradiation. FACS results and gating parameters used for quantifying Apoptosis/Necrosis in MDA-MB-231 cells after laser irradiation. DLS results for CTAB (aq.). Tables showing the DLS and zeta potential values for CTAB AuNP, Au content in cell lines, and CADA AuNPs before and after laser irradiation. Photothermal efficiency calculations for CADA AuNPs (PDF)

■ AUTHOR INFORMATION

Corresponding Author

Eden E. L. Tanner − *Department of Chemistry and Biochemistry, The University of Mississippi, University, Mississippi 38677, United States;* orcid.org/0000-0002-7919-2249; Phone: 662-915-1165; Email: eetanner@olemiss.edu

Authors

Priyavrat Vashisth − *Department of Chemistry and Biochemistry, The University of Mississippi, University, Mississippi 38677, United States*

Cameron L. Smith − *Department of Chemistry and Biochemistry, The University of Mississippi, University, Mississippi 38677, United States;* orcid.org/0000-0003-3072-028X

Dhanush L. Amarasekara − *Department of Chemistry, Mississippi State University, Mississippi State, Mississippi 39762, United States*

Gaya S. Dasanyake − *Department of Chemistry and Biochemistry, The University of Mississippi, University, Mississippi 38677, United States*

Gagandeep Singh − *Department of Chemistry and Biochemistry, The University of Mississippi, University, Mississippi 38677, United States*

Claylee M. Chism − *Department of Chemistry and Biochemistry, The University of Mississippi, University, Mississippi 38677, United States*

Christine M. Hamadani − *Department of Chemistry and Biochemistry, The University of Mississippi, University, Mississippi 38677, United States*

Tanveer Shaikh − *Department of Chemistry, Mississippi State University, Mississippi State, Mississippi 39762, United States*

Noah Grovich − *Department of Chemistry and Biochemistry, The University of Mississippi, University, Mississippi 38677, United States*

Briana Gamboa − *Department of Chemistry and Biochemistry, The University of Mississippi, University, Mississippi 38677, United States*

Nicholas C. Fitzkee − *Department of Chemistry, Mississippi State University, Mississippi State, Mississippi 39762, United States;* orcid.org/0000-0002-8993-2140

Nathan I. Hammer − *Department of Chemistry and Biochemistry, The University of Mississippi, University, Mississippi 38677, United States;* orcid.org/0000-0002-6221-2709

Complete contact information is available at: https://pubs.acs.org/10.1021/acsanm.3c04645

Notes

The authors declare no competing financial interest.

■ ACKNOWLEDGMENTS

E.E.L.T. acknowledges the College of Liberal Arts at the University of Mississippi for funding. The abstract graphic and Figure 1 was created with BioRender.com. This work was supported by the National Institutes of Health under award number R01AI139479 (NCF) and the National Science Foundation under award 1818090 (NCF). N.I.H. and C.L.S. acknowledge NSF OIA-1757220 for funding. C.M.H. acknowledges the Sigma Xi Grants-In-Aid of Research Program (#G0315202198510166) for funding. The JEOL JSM-7200 FLV FESEM at the Microscopy and Imaging Center at the University of Mississippi was funded in part by the National Science Foundation under the Major Research Instrumentation Grant 1726880. We acknowledge Glycoscience Center of Research Excellence (NIH-P20GM103460) at the University of Mississippi for providing confocal imaging facility.

■ REFERENCES

(1) Arnold, M.; Morgan, E.; Rumgay, H.; Mafra, A.; Singh, D.; Laversanne, M.; Vignat, J.; Gralow, J. R.; Cardoso, F.; Siesling, S.; Soerjomataram, I. Current and future burden of breast cancer: Global statistics for 2020 and 2040. *Breast* **2022**, *66*, 15−23.

(2) Irvin, W. J., Jr.; Carey, L. A. What is triple-negative breast cancer? *Eur. J. Cancer* **2008**, *44* (18), 2799−805.

(3) de Ruijter, T. C.; Veeck, J.; de Hoon, J. P.; van Engeland, M.; Tjan-Heijnen, V. C. Characteristics of triple-negative breast cancer. *J. Cancer Res. Clin Oncol* **2011**, *137* (2), 183−92.

(4) Zagami, P.; Carey, L. A. Triple negative breast cancer: Pitfalls and progress. *NPJ. Breast Cancer* **2022**, *8* (1), 95.

(5) Bianchini, G.; De Angelis, C.; Licata, L.; Gianni, L. Treatment landscape of triple-negative breast cancer - expanded options, evolving needs. *Nat. Rev. Clin Oncol* **2022**, *19* (2), 91−113.
(6) Zitvogel, L.; Apetoh, L.; Ghiringhelli, F.; Kroemer, G. Immunological aspects of cancer chemotherapy. *Nat. Rev. Immunol* **2008**, *8* (1), 59−73.
(7) Rakha, E. A.; El-Sayed, M. E.; Green, A. R.; Lee, A. H.; Robertson, J. F.; Ellis, I. O. Prognostic markers in triple-negative breast cancer. *Cancer* **2007**, *109* (1), 25−32.
(8) Chabner, B. A.; Roberts, T. G., Jr. Timeline: Chemotherapy and the war on cancer. *Nat. Rev. Cancer* **2005**, *5* (1), 65−72.
(9) Oun, R.; Moussa, Y. E.; Wheate, N. J. Correction: The side effects of platinum-based chemotherapy drugs: a review for chemists. *Dalton Trans* **2018**, *47* (23), 7848.
(10) Jang, S. C.; Kim, O. Y.; Yoon, C. M.; Choi, D. S.; Roh, T. Y.; Park, J.; Nilsson, J.; Lotvall, J.; Kim, Y. K.; Gho, Y. S. Bioinspired exosome-mimetic nanovesicles for targeted delivery of chemotherapeutics to malignant tumors. *ACS Nano* **2013**, *7* (9), 7698−710.
(11) Zhang, Y.; Gao, Q.; Li, W.; He, R.; Zhu, L.; Lian, Q.; Wang, L.; Li, Y.; Bradley, M.; Geng, J. Controlled Intracellular Polymerization for Cancer Treatment. *JACS Au* **2022**, *2* (3), 579−589.
(12) Pan, Y.; Ma, X.; Liu, C.; Xing, J.; Zhou, S.; Parshad, B.; Schwerdtle, T.; Li, W.; Wu, A.; Haag, R. Retinoic Acid-Loaded Dendritic Polyglycerol-Conjugated Gold Nanostars for Targeted Photothermal Therapy in Breast Cancer Stem Cells. *ACS Nano* **2021**, *15* (9), 15069−15084.
(13) Huang, X.; Jain, P. K.; El-Sayed, I. H.; El-Sayed, M. A. Plasmonic photothermal therapy (PPTT) using gold nanoparticles. *Lasers Med. Sci.* **2008**, *23* (3), 217−28.
(14) Melamed, J. R.; Edelstein, R. S.; Day, E. S. Elucidating the fundamental mechanisms of cell death triggered by photothermal therapy. *ACS Nano* **2015**, *9* (1), 6−11.
(15) Li, X.; Gao, Y.; Li, H.; Majoral, J.-P.; Shi, X.; Pich, A. Smart and bioinspired systems for overcoming biological barriers and enhancing disease theranostics. *Prog. Mater. Sci.* **2023**, *140*, No. 101170.
(16) Lu, Y.; Luo, Q.; Jia, X.; Tam, J. P.; Yang, H.; Shen, Y.; Li, X. Multidisciplinary strategies to enhance therapeutic effects of flavonoids from Epimedii Folium: Integration of herbal medicine, enzyme engineering, and nanotechnology. *Journal of Pharmaceutical Analysis* **2023**, *13*, 239−254.
(17) Jia, J.; Liu, G.; Xu, W.; Tian, X.; Li, S.; Han, F.; Feng, Y.; Dong, X.; Chen, H. Fine-Tuning the Homometallic Interface of Au-on-Au Nanorods and Their Photothermal Therapy in the NIR-II Window. *Angew. Chem., Int. Ed. Engl.* **2020**, *59* (34), 14443−14448.
(18) Ren, Y.; Yan, Y.; Qi, H. Photothermal conversion and transfer in photothermal therapy: From macroscale to nanoscale. *Adv. Colloid Interface Sci.* **2022**, *308*, No. 102753.
(19) Zhang, Y.; Zhan, X.; Xiong, J.; Peng, S.; Huang, W.; Joshi, R.; Cai, Y.; Liu, Y.; Li, R.; Yuan, K.; Zhou, N.; Min, W. Temperature-dependent cell death patterns induced by functionalized gold nanoparticle photothermal therapy in melanoma cells. *Sci. Rep* **2018**, *8* (1), 8720.
(20) Zhang, A.; Zhang, Y.; Liu, Z.; Huang, G.; Wu, L.; Fu, Y.; Wang, X.; Du, Y. Anisotropic Gold Nanostructures Applied to Improve Solar Energy Conversion. *Applied Materials Today* **2022**, *29*, No. 101575.
(21) Riley, R. S.; Day, E. S. Gold nanoparticle-mediated photothermal therapy: applications and opportunities for multimodal cancer treatment. *Wiley Interdiscip Rev. Nanomed Nanobiotechnol* **2017**, *9* (4), na DOI: 10.1002/wnan.1449.
(22) Ortiz-Castillo, J. E.; Gallo-Villanueva, R. C.; Madou, M. J.; Perez-Gonzalez, V. H. Anisotropic Gold Nanoparticles: A Survey of Recent Synthetic Methodologies. *Coord. Chem. Rev.* **2020**, *425*, No. 213489.
(23) Li, N.; Zhao, P.; Astruc, D. Anisotropic gold nanoparticles: synthesis, properties, applications, and toxicity. *Angew. Chem., Int. Ed. Engl.* **2014**, *53* (7), 1756−89.
(24) Alkilany, A. M.; Murphy, C. J. Toxicity and cellular uptake of gold nanoparticles: what we have learned so far? *J. Nanopart. Res.* **2010**, *12* (7), 2313−2333.
(25) Khafaji, M.; Bavi, O.; Zamani, M. Gold-based hybrid nanostructures: more than just a pretty face for combinational cancer therapy. *Biophys Rev.* **2022**, *14* (1), 317−326.
(26) Chen, Y.; Xianyu, Y.; Jiang, X. Surface Modification of Gold Nanoparticles with Small Molecules for Biochemical Analysis. *Acc. Chem. Res.* **2017**, *50* (2), 310−319.
(27) Eyckens, D. J.; Henderson, L. C. A Review of Solvate Ionic Liquids: Physical Parameters and Synthetic Applications. *Front Chem.* **2019**, *7*, 263.
(28) Keul, H. A.; Ryu, H. J.; Moller, M.; Bockstaller, M. R. Anion effect on the shape evolution of gold nanoparticles during seed-induced growth in imidazolium-based ionic liquids. *Phys. Chem. Chem. Phys.* **2011**, *13* (30), 13572−8.
(29) Ryu, H. J.; Sanchez, L.; Keul, H. A.; Raj, A.; Bockstaller, M. R. Imidazolium-based ionic liquids as efficient shape-regulating solvents for the synthesis of gold nanorods. *Angew. Chem., Int. Ed. Engl.* **2008**, *47* (40), 7639−43.
(30) Dinda, E.; Si, S.; Kotal, A.; Mandal, T. K. Novel ascorbic acid based ionic liquids for the in situ synthesis of quasi-spherical and anisotropic gold nanostructures in aqueous medium. *Chemistry* **2008**, *14* (18), 5528−37.
(31) Consoli, G. M. L.; Forte, G.; Maugeri, L.; Consoli, V.; Sorrenti, V.; Vanella, L.; Buscarino, G.; Agnello, S.; Camarda, M.; Granata, G.; Ferreri, L.; Petralia, S. Near-Infrared-Responsive Choline-Calix [4] arene-Gold Nanostructures for Potential Photothermal Cancer Treatment. *ACS Applied Nano Materials* **2023**, *6* (1), 358−369.
(32) Singh, G.; Dasanayake, G. S.; Chism, C. M.; Vashisth, P.; Kaur, A.; Misra, S. K.; Sharp, J. S.; Tanner, E. Good's buffer based highly biocompatible ionic liquid modified PLGA nanoparticles for the selective uptake in cancer cells. *Materials Chemistry Frontiers* **2023**, *7*, 6213.
(33) Singh, G.; Kaur, M.; Kaur, H.; Kang, T. S. Synthesis and Complexation of a New Caffeine Based Surface Active Ionic Liquid with Lysozyme in Aqueous Medium: Physicochemical, Computational and Antimicrobial Studies. *J. Mol. Liq.* **2021**, *325*, No. 115156.
(34) Curreri, A. M.; Mitragotri, S.; Tanner, E. E. L. Recent Advances in Ionic Liquids in Biomedicine. *Adv. Sci. (Weinh)* **2021**, *8* (17), No. e2004819.
(35) Singh, G.; Kaur, M.; Singh, D.; Kesavan, A. K.; Kang, T. S. Antimicrobial Colloidal Complexes of Lysozyme with Bio-Based Surface Active Ionic Liquids in Aqueous Medium. *J. Phys. Chem. B* **2020**, *124* (18), 3791−3800.
(36) Tanner, E. E. L.; Curreri, A. M.; Balkaran, J. P. R.; Selig-Wober, N. C.; Yang, A. B.; Kendig, C.; Fluhr, M. P.; Kim, N.; Mitragotri, S. Design Principles of Ionic Liquids for Transdermal Drug Delivery. *Adv. Mater.* **2019**, *31* (27), No. e1901103.
(37) Liu, H.; Yu, H. Ionic Liquids for Electrochemical Energy Storage Devices Applications. *Journal of Materials Science & Technology* **2019**, *35* (4), 674−686.
(38) Ibsen, K. N.; Ma, H.; Banerjee, A.; Tanner, E. E. L.; Nangia, S.; Mitragotri, S. Mechanism of Antibacterial Activity of Choline-Based Ionic Liquids (CAGE). *ACS Biomater Sci. Eng.* **2018**, *4* (7), 2370−2379.
(39) Agatemor, C.; Ibsen, K. N.; Tanner, E. E. L.; Mitragotri, S. Ionic liquids for addressing unmet needs in healthcare. *Bioeng Transl Med.* **2018**, *3* (1), 7−25.
(40) Hallett, J. P.; Welton, T. Room-temperature ionic liquids: solvents for synthesis and catalysis. 2. *Chem. Rev.* **2011**, *111* (5), 3508−76.
(41) Li, X.; Hetjens, L.; Wolter, N.; Li, H.; Shi, X.; Pich, A. Charge-reversible and biodegradable chitosan-based microgels for lysozyme-triggered release of vancomycin. *Journal of Advanced Research* **2023**, *43*, 87−96.
(42) Singh, G.; Kaur, M.; Aswal, V. K.; Kang, T. S. Aqueous colloidal systems of bovine serum albumin and functionalized surface active ionic liquids for material transport. *RSC Adv.* **2020**, *10* (12), 7073−7082.
(43) Blusztajn, J. K. Choline, a vital amine. *Science* **1998**, *281* (5378), 794−5.

(44) Giovannini, E.; Lazzeri, P.; Milano, A.; Gaeta, M. C.; Ciarmiello, A. Clinical applications of choline PET/CT in brain tumors. *Curr. Pharm. Des* **2014**, *21* (1), 121−7.
(45) Nikoobakht, B.; El-Sayed, M. A. Preparation and Growth Mechanism of Gold Nanorods (NRs) Using Seed-Mediated Growth Method. *Chem. Mater.* **2003**, *15* (10), 1957−1962.
(46) Jana, N. R.; Gearheart, L.; Murphy, C. J. Wet Chemical Synthesis of High Aspect Ratio Cylindrical Gold Nanorods. *J. Phys. Chem. B* **2001**, *105* (19), 4065−4067.
(47) Chism, C. M.; Plash, S.; Zuckerman, D.; Dasanayake, G. S.; Bennett, M.; Tripathi, S. K.; Pedigo, S. D.; Tanner, E. E. L. Antimicrobial Effects of Anion Manipulation with Biocompatible Choline Carboxylic Acid-Based Ionic Liquids. *ACS Applied Engineering Materials* **2023**, *1* (1), 23−31.
(48) Damiano, F.; De Benedetto, G. E.; Longo, S.; Giannotti, L.; Fico, D.; Siculella, L.; Giudetti, A. M. Decanoic Acid and Not Octanoic Acid Stimulates Fatty Acid Synthesis in U87MG Glioblastoma Cells: A Metabolomics Study. *Front Neurosci* **2020**, *14*, 783.
(49) Huang, W. C.; Tsai, T. H.; Chuang, L. T.; Li, Y. Y.; Zouboulis, C. C.; Tsai, P. J. Anti-bacterial and anti-inflammatory properties of capric acid against Propionibacterium acnes: a comparative study with lauric acid. *J. Dermatol Sci.* **2014**, *73* (3), 232−40.
(50) Busbee, B.D.; Obare, S.O.; Murphy, C.J. An Improved Synthesis of High-Aspect-Ratio Gold Nanorods. *Adv. Mater.* **2003**, *15* (5), 414−416.
(51) Maxit, B.; Catros, C.; Aubrit, F.; Le Mener, J.; Sandre, O.; Jacob, D.; Boj, S. New methodology for anisotropic nanoparticles characterization by polarization light scattering: length and diameter determination of rod-like nanoparticles. In *Conference of Science & Technology for Integrated Circuits (CSTIC2024)−Symposium VI: Metrology, Reliability and Testing*, 2024.
(52) Ragheb, R.; Nobbmann, U. Multiple scattering effects on intercept, size, polydispersity index, and intensity for parallel (VV) and perpendicular (VH) polarization detection in photon correlation spectroscopy. *Sci. Rep.* **2020**, *10* (1), 21768.
(53) Canbek Ozdil, Z. C.; Spalla, O.; Menguy, N.; Testard, F. Competitive Seeded Growth: An Original Tool to Investigate Anisotropic Gold Nanoparticle Growth Mechanism. *J. Phys. Chem. C* **2019**, *123* (41), 25320−25330.
(54) Jain, T.; Tehrani-Bagha, A. R.; Shekhar, H.; Crawford, R.; Johnson, E.; Nørgaard, K.; Holmberg, K.; Erhart, P.; Moth-Poulsen, K. Anisotropic growth of gold nanoparticles using cationic gemini surfactants: effects of structure variations in head and tail groups. *Journal of Materials Chemistry C* **2014**, *2* (6), 994−1003.
(55) Aioub, M.; El-Sayed, M. A. A real-time surface enhanced raman spectroscopy study of plasmonic photothermal cell death using targeted gold nanoparticles. *J. Am. Chem. Soc.* **2016**, *138* (4), 1258−1264.
(56) Aioub, M.; Kang, B.; Mackey, M. A.; El-Sayed, M. A. Biological targeting of plasmonic nanoparticles improves cellular imaging via the enhanced scattering in the aggregates formed. *J. Phys. Chem. Lett.* **2014**, *5* (15), 2555−2561.
(57) Jain, P. K.; El-Sayed, M. A. Surface plasmon coupling and its universal size scaling in metal nanostructures of complex geometry: elongated particle pairs and nanosphere trimers. *J. Phys. Chem. C* **2008**, *112* (13), 4954−4960.
(58) Almada, M.; Leal-Martínez, B.; Hassan, N.; Kogan, M.; Burboa, M.; Topete, A.; Valdez, M.; Juárez, J. Photothermal conversion efficiency and cytotoxic effect of gold nanorods stabilized with chitosan, alginate and poly (vinyl alcohol). *Materials Science and Engineering* **2017**, *77*, 583−593.
(59) Lin, M.; Guo, C.; Li, J.; Zhou, D.; Liu, K.; Zhang, X.; Xu, T.; Zhang, H.; Wang, L.; Yang, B. J. A. a. m. interfaces, Polypyrrole-coated chainlike gold nanoparticle architectures with the 808 nm photothermal transduction efficiency up to 70%. *ACS Appl. Mater. Interfaces* **2014**, *6* (8), 5860−5868.
(60) Wang, Y.; Black, K. C. L.; Luehmann, H.; Li, W.; Zhang, Y.; Cai, X.; Wan, D.; Liu, S.-Y.; Li, M.; Kim, P.; Li, Z.-Y.; Wang, L. V.; Liu, Y.; Xia, Y. *Comparison study of gold nanohexapods, nanorods, and nanocages for photothermal cancer treatment* **2013**, *7* (3), 2068−2077.
(61) Huang, X.; El-Sayed, M. Gold nanoparticles: Optical properties and implementations in cancer diagnosis and photothermal therapy. *Journal of advanced research* **2010**, *1* (1), 13−28.
(62) Yasun, E.; Li, C.; Barut, I.; Janvier, D.; Qiu, L.; Cui, C.; Tan, W. BSA modification to reduce CTAB induced nonspecificity and cytotoxicity of aptamer-conjugated gold nanorods. *Nanoscale* **2015**, *7* (22), 10240−8.
(63) Wang, L.; Jiang, X.; Ji, Y.; Bai, R.; Zhao, Y.; Wu, X.; Chen, C. Surface chemistry of gold nanorods: origin of cell membrane damage and cytotoxicity. *Nanoscale* **2013**, *5* (18), 8384−91.
(64) Cui, X.; Mao, S.; Liu, M.; Yuan, H.; Du, Y. Mechanism of surfactant micelle formation. *Langmuir* **2008**, *24* (19), 10771−10775.
(65) Lin, J.; Zhang, H.; Chen, Z.; Zheng, Y. Penetration of lipid membranes by gold nanoparticles: insights into cellular uptake, cytotoxicity, and their relationship. *ACS Nano* **2010**, *4* (9), 5421−5429.
(66) Jing, B.; Lan, N.; Qiu, J.; Zhu, Y. Interaction of ionic liquids with a lipid bilayer: a biophysical study of ionic liquid cytotoxicity. *J. Phys. Chem. B* **2016**, *120* (10), 2781−2789.
(67) Ding, L.; Yao, C.; Yin, X.; Li, C.; Huang, Y.; Wu, M.; Wang, B.; Guo, X.; Wang, Y.; Wu, M. Size, shape, and protein corona determine cellular uptake and removal mechanisms of gold nanoparticles. *Small* **2018**, *14* (42), No. 1801451.
(68) Maxfield, F. R. Plasma membrane microdomains. *Curr. Opin. Cell Biol.* **2002**, *14* (4), 483−487.
(69) Adjei, I. M.; Sharma, B.; Labhasetwar, V. Nanoparticles: cellular uptake and cytotoxicity. *Nanomaterial: impacts on cell biology and medicine* **2014**, *811*, 73−91.
(70) Wang, S. H.; Lee, C. W.; Chiou, A.; Wei, P. K. Size-dependent endocytosis of gold nanoparticles studied by three-dimensional mapping of plasmonic scattering images. *J. Nanobiotechnology* **2010**, *8*, 33.
(71) Li, Y.; Monteiro-Riviere, N. A. Mechanisms of cell uptake, inflammatory potential and protein corona effects with gold nanoparticles. *Nanomedicine* **2016**, *11* (24), 3185−3203.
(72) Song, A. S.; Najjar, A. M.; Diller, K. R. Thermally induced apoptosis, necrosis, and heat shock protein expression in three-dimensional culture. *Journal of biomechanical engineering* **2014**, *136* (7), No. 071006.
(73) Rock, K. L.; Kono, H. The inflammatory response to cell death. *Annu. Rev. Pathol. Mech.* **2008**, *3*, 99−126.

https://doi.org/10.1021/acsanm.3c04645
ACS Appl. Nano Mater. 2024, 7, 26332−26343